



1 **Atmospheric nanoparticles hygroscopic**
2 **growth measurement by combined surface**
3 **plasmon resonance microscope and**
4 **hygroscopic-tandem differential mobility**
5 **analyzer**

6 Zhibo Xie^{a,b,c}, Jiaoshi Zhang^{a,1*}, Huaqiao Gui^{a,c*}, Yang Liu^d, Bo Yang^a, Haosheng Dai^a,
7 Hang Xiao^{b,c}, Douguo Zhang^d, Da-Ren Chen^e, Jianguo Liu^{a,b,c}.

8 ^a *Key Laboratory of Environmental Optics and Technology, Anhui Institute of Optics and*
9 *Fine Mechanics, Chinese Academy of Sciences, Hefei 230031, China*

10 ^b *Innovation excellence center for urban atmospheric environment of CAS, Institute of*
11 *Urban Environment, Chinese Academy of Sciences, Xiamen, 361021, China*

12 ^c *University of Chinese Academy of Sciences, Beijing, 100049, China*

13 ^d *Institute of Photonics, Department of Optics and Optical Engineering, University of*
14 *Science and Technology of China, Hefei, Anhui 230026, China.*

15 ^e *Particle Laboratory, Department of Mechanical and Nuclear Engineering, Virginia*
16 *Commonwealth University, 401 West Main Street, Richmond, VA 23284.*

17 ¹ *now at Center for Aerosol Science and Engineering, Washington University in St. Louis,*
18 *St. Louis, Missouri, USA.*

19 * Corresponding author: Jiaoshi Zhang (jszhang@aiofm.ac.cn) and Huaqiao Gui
20 (hqgui@aiofm.ac.cn)

21

22 **ABSTRACT**

23 The hygroscopic growth of atmospheric aerosols plays an important role in regional



24 radiation, cloud formation and hence climate. Aerosol hygroscopic growth is often
25 characterized by humidified tandem differential mobility analyzers (HTDMA), and Xie et
26 al. (2020) recently demonstrated that hygroscopic growth measurements of single-particle
27 are possible using a surface plasmon resonance microscope-azimuthal rotation illumination
28 (SPRM-ARI). The hygroscopic properties of ambient aerosols are not uniform and often
29 exhibit large RH and size variabilities, due to different chemical compositions and mixing
30 states. To better understand the contribution of different aerosol components and establish
31 the link between the apparent hygroscopic properties of bulk aerosols and single-particle,
32 we conduct combined hygroscopic growth measurements of single-particle by a SPRM-
33 ARI and bulk particles by an HTDMA. The atmospheric nanoparticles were grouped into
34 four subgroups labeled as EC, fly ash, OC and AS+OC based on the energy dispersive
35 spectroscope results (Experimental information: 100nm~200nm, at noon, September 28th,
36 2021 and March 22th, 2022 in Hefei China). The relationship between the chemical
37 composition of a single nanoparticle in each subgroup and its hygroscopicity was
38 characterized using SPRM-ARI. Then, the HTDMA data were shown to be fitted and
39 reconstructed by the constitutive particle size distributions calculated by the SPRM-ARI
40 measured GFs (growth factor), and the percentage of four subgroups in atmospheric
41 particles could also be found through the fitting. Based on the test results, we found the OC
42 content of AS+OC nanoparticles increased with the increase of particle size, and the OC
43 condensation may play a promoting role in the particle growth process. Lastly, this fitting
44 reconstruction method has a good correlation with the quantitative results of membrane
45 sampling, and can be used for reference to analyze the contribution of particle
46 hygroscopicity and the growth mechanism of nanoparticle.

47

48 **Keywords:** single atmospheric aerosols, hygroscopic growth, surface plasmon,
49 nanoparticles, in situ imaging.

50



51 **1. Introduction**

52 The hygroscopicity of aerosol particles plays an important role in the haze and cloud
53 formation, and the climate change in the solar radiation and precipitation (Sloane and Wolff,
54 1985; Penner et al., 1993). Aerosols can be simply classified as hygroscopic and non-
55 hygroscopic aerosols, which denotes the ability of aerosol particles to form a haze or cloud
56 (Abbatt et al., 2005). In addition, aerosol hygroscopicity can be further complicated due to
57 the mixing or/and heterogeneous reaction of aerosol particles, consequently affecting their
58 abilities in the solar radiation absorption and cloud formation (Shi et al., 2012; Pilinis et
59 al., 1995; Agarwal et al., 2010). The recent research on the atmospheric convective clouds
60 in the Amazon area has shown that nanoparticles can rapidly deliquesce and form the
61 clouds, which further enhances atmospheric convection and promotes the precipitation
62 (Fan et al., 2018). Because of the high concentration, the hygroscopic property of these
63 nanoparticles and its potential contribution to the cloud condensation is believed significant
64 (Tan et al., 2017). It thus becomes very important to understand the relationship between
65 the physicochemical property and the hygroscopic property of these nanoparticles, and the
66 contribution of the above relationship to the overall aerosol hygroscopicity growth process.

67 The technology for the hygroscopic growth characteristics of aerosols can be classified
68 as: ensemble particle and single-particle. A hygroscopic-tandem differential mobility
69 analyzer (HTDMA) commonly uses to measure the hygroscopic growth of multiple
70 particles in a specific electrical mobility size (Lei et al., 2014; Lei et al., 2018). Although
71 the HTDMA is reliable, the sizes of particles which could be analyzed is typically less than
72 300 nm (due to the DMA design) and the measured data represent the average of an
73 ensemble particle. For polydisperse particles, the result measured by the ensemble particle
74 technique is the overall average of multiple particle measurements. The technique cannot
75 be used to measure the hygroscopic growth of particles in the large sizes of the size
76 distribution, which has significant contribution to the visibility, weather and climate studies,
77 but cannot be represented by the average (Morris et al., 2016). In contrast, the single-



78 particle technique offers the qualitative characterization of moisture absorption change due
79 to the chemical composition and material phase of individual particles (Krieger et al., 2012).
80 Depending on the particle capture methods, the single-particle hygroscopic growth
81 imaging technologies can be grouped as the plate-deposition imaging and suspension
82 imaging (Hiranuma et al., 2008; Peng et al., 2001). The plate-deposition imaging by
83 traditional 2D imaging methods (*e.g.*, Raman spectroscopy; environmental scanning
84 electron microscopy, ESEM; surface-enhanced Raman spectroscopy) will be affected by
85 the imaging angle and orientation (Ebert et al., 2002; Gupta et al., 2015; Craig et al., 2015;
86 Gen et al., 2017), making it difficult to measure the height change of imaging particles after
87 the hygroscopic growth. The particle imaging by the current 3D method (*i.e.*, atomic force
88 microscopy) requires to scan the imaging particle for a long time period, resulting in a long
89 measurement time and increasing the chance of particle puncture by the scanning probe
90 (Harmon et al., 2010; Morris et al., 2015). Without the issue encountered in the plate-
91 deposition imaging (Braun et al., 2001; Lv et al., 2018), the suspension imaging methods
92 (*i.e.*, electric balance, optical tweezers) are however limited for particles in the sizes larger
93 than 500 nm, making it very challenging to measure the size change of nanoparticles during
94 the hygroscopic growth. More, it is difficult to assess the contribution of the hygroscopic
95 characteristics of single-particle in the atmosphere by the single-particle techniques (Li et
96 al., 2017; Mikhailov et al., 2015). Although ESEM/environmental transmission electron
97 microscopy (ETEM) can be used to estimate the concentrations of nanoparticles by
98 counting them on the ESEM/ETEM images, the process is very time-consuming and only
99 limited numbers of particles being counted. An efficient and accurate method for
100 measuring the hygroscopic growth of an ensemble of atmospheric particles is required to
101 overcome the deficiencies experienced in the current methods.

102 The surface plasmon resonance microscopy (SPRM) can continuously perform the
103 imaging measurements of single binding events (Wang et al., 2010; Huang et al.,) and the
104 light intensity is directly related to the volume of the object (without the photo-bleaching



105 and fluorophore scintillation) (Young et al., 2018; Halpern et al., 2014). SPRM has been
106 used widely in the research involving biological targets (including cells, bacteria, viruses,
107 DNA molecules and proteins) and the local electrochemical reactions and catalytic
108 reactions of nanomaterials (Syal et al., 2016; Maley et al., 2016; Wang et al., 2012). More,
109 the influence of the relative humidity on SPRM is very minor, *i.e.*, the imaging is not
110 affected by the water vapor on the imaging particle surface (Fang et al., 2016). In the
111 previous study, we used the azimuthal rotation illumination (ARI) to improve the single-
112 direction SP imaging resolution, which enables a clear imaging of 50 nm PSL particles
113 (Kuai et al., 2019). The *in situ* SPRM-ARI imaging method was then applied to measure
114 the hygroscopic growth of 90 nm lab-generated particles (Xie et al., 2020). The above
115 example demonstrates that the SPRM-ARI can distinguish the size change of particles in
116 the sizes less than the diffraction limit of the illumination light and accurately characterize
117 the volume change ratio of nanoparticles after the hygroscopic growth (Kuai et al., 2020).
118 Therefore, using the SPRM-ARI to perform an accurate hygroscopicity measurement of
119 atmospheric single nanoparticles and comparing it with the data measured by HTDMA are
120 expected to provide a rapid method to measure the contribution of hygroscopicity of
121 individual atmospheric particles to the overall hygroscopic growth of atmospheric particles.

122 In this work, the *in situ* SPRM-ARI imaging method was used in combination with the
123 HTDMA technique to characterize the hygroscopic growth of atmospheric nanoparticles
124 in the sizes of 100, 150 and 200 nm. The chemical compositions of atmospheric
125 nanoparticles were measured by the scanning electron microscopy (SEM) with an energy
126 dispersive spectrometer (EDS) and quartz-filter sampling analysis. By recombining the
127 results measured by the HTDMA and the *in situ* SPRM-ARI, a rapid method was developed
128 to characterize the hygroscopic contribution of different subgroups atmospheric
129 nanoparticles.

130

131 2. Materials and methods



132 **2.1 Atmospheric nanoparticle collection and component analysis.**

133 The collection of atmospheric nanoparticles was conducted at the Hefei Institute of
134 Physical Science (Figure S1), Chinese Academy of Sciences, in Hefei, China (31° 54' 31"
135 N, 117° 9' 36" E) at the noon of September 28th, 2021 and March 22th, 2022. As shown in
136 Figure S1, the site is located in the northwest of Hefei City, where both high-temperature
137 heat sources (thermal power plants) and residential areas are present. The collected
138 nanoparticles can be considered as representative nanoparticles of inland cities in China.

139 As shown in Figure 1a, the sampled atmospheric particles were passed through a
140 diffusion dryer (TSI 3062) to reduce the relative humidity of sampled stream. Particles with
141 the electrical mobility sizes of 100, 150 and 200 nm were selected by a DMA (TSI 3081)
142 operated by the DMA platform (TSI 3080). The atmospheric nanoparticles size distribution
143 in the above two days was shown in Figure S2, and the median particle size was in the
144 range of 100~150nm, which was consistent with the settled screening particle size.

145 For atmospheric nanoparticle on September 28th, 2021, classified particles were
146 collected on the substrate surface in the sample cell. Substrates of two types (in the same
147 size) were used: one is with the 45-nm-thickness gold coating, which is used for the *in situ*
148 SPRM-ARI hygroscopic growth measurement, and the other is commercial silicon wafer
149 used for the SEM measurement. The gold-coated surface (with thickness deviation of $\pm 5\%$
150 within a 4 in² area) was prepared by an e-beam evaporator (K.J. Lesker, Lab 18) on a
151 standard microscope cover glass (thickness: 0.17 mm) at a vacuum pressure of $<10^{-3}$ mTorr.
152 The size and element distributions of atmospheric nanoparticles were measured by the
153 SEM (SU8220, Hitachi, Japan) with an EDS (Aztec, Oxford, UK).

154 For atmospheric nanoparticle on March 22th, 2022, except the gold coating substrate, the
155 nanoparticles screened by DMA were collected by quartz filter (Tisch Environmental TE-
156 20-301QZ). The sampling flow was 1.5L/min, and the collected nanoparticles were used
157 for organic carbon (OC), elemental carbon (EC) and SO₄²⁻ content measurement. The
158 content of OC and EC were measured by the traditional thermo-optical method (Chow et



159 al., 2004). In the environment of pure gas He and mixed gas He/O₂, the quartz filter
160 membrane was heated gradually, and the CO₂ produced by catalytic oxidation was
161 quantitatively analyzed by laser detector (Ding et al., 2014). For the SO₄²⁻ measurement,
162 the quartz filter membranes with atmospheric nanoparticles were extracted with organic-
163 free Milli-Q water (Direct-Q3, Millipore) using an ultrasonic bath for 20 min, and the
164 content of SO₄²⁻ in the extract was measured by ion chromatography (ICS-3000, Dionex).
165 The concentration of OC, EC, and SO₄²⁻ reported here were corrected by the blank
166 membrane, and the concentration was converted into μg/m³.

167 **2.2 SPRM-ARI hygroscopicity measurement system.**

168 As shown in Figure 1a, a Nafion dryer, a Nafion humidifier (Perma Pure, USA) and a
169 proportional-integral-differential (PID) controller were used to control the relative
170 humidity in the sample cell. The Nafion exchangers enables users to obtain the dry gas (5%
171 RH) and the wet gas (95%RH). A close loop control with the feedback of measured RH of
172 the gas (via a RH sensor) was applied by varying the mixing ratio of dry and wet gases to
173 achieve the set RH. The mixed gas with the desired RH is then directed into the sample
174 cell to humidify the DMA-classified atmospheric nanoparticles deposited on the Au-coated
175 surface. The particle deposition and humidification processes were consequently
176 performed via a two-way switch valve to reduce the interference of impurities during the
177 growth measurement.

178 Also shown in Figure 1a is the schematic diagram of the *in situ* SPRM-ARI system,
179 where the illumination source is a 635 nm parallel laser with the power of 54 mW. Two
180 orthogonal polarizers are used to eliminate reflected laser signals, allowing the surface
181 plasmon (SP) signals to be collected as far as possible via a charge-coupled device camera
182 (Andor, Neo, UK). Using an objective (100×, numerical aperture (NA) of 1.49; Nikon,
183 Japan) and a pair of scanning galvanometers, the laser beams could be focused on any
184 position in the back focal plane (BFP). In this configuration (as shown in Figure 1b), the
185 laser beam can rotate around the Au film at a specific angle (θ), which is called as the



186 azimuthal rotational illumination. Figure S3 shows the reflection BFP image of the 45 nm
187 Au film. The presence of the symmetrical dark arc on the image verified the existence of
188 the p-polarized SPs. The SP signals of atmospheric nanoparticles on the Au film were
189 recorded as the cell RH was increased. Under the ARI mode, split circular spots are formed
190 if the particle size is less than the diffraction limit. By combining with the information of
191 the DMA classification and SEM measurement, the initial sizes of selected atmospheric
192 nanoparticles can be clearly determined (Xie et al., 2020). The statistics of the gray
193 intensity (GI) on the SP images is applied for the SP image processing (Huang et al., 2007).
194 It is because the GI is positively correlated with the volumes of imaging particles, and the
195 GF (growth factor) of imaging atmospheric nanoparticles can be obtained by the cube root
196 of the GI.

197 For the reference to the Köhler theory (Petters et al., 2007; Fan et al., 2020), the
198 hygroscopicity parameter κ can be calculated using the GF measured by the SPRM-ARI
199 system.

$$200 \quad \kappa = \left(\frac{\exp\left(\frac{A}{D_d Gf}\right)}{RH} - 1 \right) (Gf^3 - 1) \quad (1)$$

$$201 \quad A = \frac{4\sigma_{s/a}M_w}{RT\rho_w} \quad (2)$$

202 where Gf is the growth factor measured using the SPRM-ARI system, D_d is the dry
203 diameter of the atmospheric particles, RH is the relative humidity in the sample cell (RH:
204 84%) and $\sigma_{s/a}$ is the surface tension of the solution/air interface ($s/a=0.0728 \text{ Nm}^{-2}$). M_w is
205 the molecular weight of water, R is the universal gas constant, T is the environmental
206 temperature (298 K) and ρ_w is the water density. The deliquescence droplet was selected
207 as the default well-mixed solution. Note that the Zdanovskii-Stokes-Robinson (ZSR)
208 model was not used to calculate the k value because of the complex chemical composition
209 of atmospheric particles.

210 **2.3 HTDMA**

211 The HTDMA was used to measure the hygroscopic growth of the above two days
212 atmospheric nanoparticles in a narrow electrical mobility size distribution as those



213 measured using SPRM-ARI. Figure S4 shows the HTDMA including a long DMA (TSI
214 3081), a humidification chamber and a scanning mobility particle sizer (TSI DMA 3081
215 and WCPC 3788) system. After passing through the diffusion dryer and particle charge
216 neutralizer, atmospheric particles were introduced into the DMA1 to select atmospheric
217 particles in the electrical mobility sizes of 100 nm, 150 nm and 200 nm. Atmospheric
218 particles in the selected sizes were humidified in a Nafion pipe (at the flow rate of 0.3
219 L/min) with a sheath gas whose RH is controlled in the same manner as that in the SPRM-
220 ARI humidification system. The same RH-controlled gas was also used for the sheath flow
221 for the DMA2 operation. The sheath gas of the DMA2 was circulated via an air pump with
222 an air filter (Parker 9922-11-AQ).

223

224 **3. Results and discussion**

225 **3.1 Combined SPRM-HTDMA measurements of 100 nm ambient aerosols**

226 Figure 2 shows the SEM images of typical 100nm particles and their EDS mapping results
227 on September 28th, 2021. According to the morphology and EDS mapping, atmospheric
228 particles were grouped into four subgroups labeled as: EC (Figure 2a), OC (Figure 2b), fly
229 ash (Figure 2c) and AS+OC (ammonium sulfate) (Figure 2d). The EDS of the 100 nm
230 atmospheric nanoparticles (given in Figure 2a) showed the dominant C element signal and
231 no obvious presence of the O element signal. It can be concluded that the 100 nm
232 atmospheric particulate shown in Figure 2a shall be in the EC group, which are mainly
233 produced by the incomplete combustion of fossil fuels (Jacobson et al., 2000). As for
234 nanoparticles in the OC group (in Figure 2b), an obvious O element signal was present in
235 addition to the obvious C element signal. The sources of OC particles are very diverse. The
236 OC particles could be either from the direct emission of pollution sources or the secondary
237 formation of atmospheric volatile organic compounds (VOCs) (Zhang et al., 2017). In
238 Figure 2c, the EDS mapping was mainly the Fe and O element signals. Note that the Si
239 element signal cannot be used to identify the particles because of the Si substrate. The



240 particle morphology in Figure 2c shows a cluster of spherical particles, and the Fe and O
241 element signals are evenly distributed over the whole SEM-ed particle. The particle shown
242 in Figure 2c is thus grouped as fly ash. The source of fly ash particles is likely from the
243 high temperature combustion (Bondy et al., 2018). Atmospheric nanoparticles, shown in
244 Figure 2d, are ones containing OA and AS particles, which are widely distributed in rural
245 and urban areas. The EDS of the OA+AS particles shows obvious S element signals in
246 addition to the C and O element signals. The unique characteristics of the particle
247 morphology (shown in Figure 2d) is the brighter color, which is due to the presence of
248 sulfate (because of the high conductivity of AS particles). The image also evidenced that
249 the mixing of OC and AS in the particle is not uniform in 100nm atmospheric nanoparticles.

250 Figure 3 shows the measurement of the hygroscopic growth of 100 nm atmospheric
251 particles by *in situ* SPRM-ARI. The SPRM grayscale images are provided at the RH levels
252 of 30%, 60%, 80% and 90%. By collecting the GI of the SPRM images under various RH
253 conditions, the cube root ratio of the GI can represent the GF for the particle moisture
254 absorption growth. It is found that, during the hygroscopic growth process of 100 nm
255 atmospheric nanoparticles, the *in situ* SPRM-ARI results were split circular spots, similar
256 to those obtained for the previous *in situ* SPRM-ARI obtained for the hygroscopic growth
257 of nanoparticles in a pure composition (Xie et al., 2020; Kuai et al., 2020). The above
258 observation also indicates that the atmospheric nanoparticles involved in this work were
259 less than the diffraction limit. The size of the measured particles was determined to be 100
260 nm by SEM.

261 As the RH increased, the *in situ* SPRM-ARI results can be grouped into three growth
262 types depending on the GI variation. In the first growth type, the GI did not obviously
263 change, and the speckled spots on the SPRM images basically remained their shapes at low
264 RH, indicating that the GF of this 100 nm atmospheric particle did not change as the RH
265 increased. According to the previous experience, this series of *in situ* SPRM-ARI results
266 should be for particles either in the EC or fly ash group. In the second growth type, the GI



267 of split circular spots was gradually changed, *i.e.*, the GI of the spots slowly increased while
268 the circular spots remained segmented, indicating the size of the atmospheric particle
269 during the hygroscopic growth remained less than the diffraction limit. Compared to that
270 obtained for particles in the first growth type, the SPRM-ARI results of particles in this
271 type shows the brightness of the spots had been increased. In other words, the GF of
272 atmospheric particles in this group was small, and their sizes were slowly increased during
273 the hygroscopic growth. The GF of this nanoparticle was 1.25 when the RH reached 90%.
274 Based on the previous result⁴², this atmospheric particle should be in the OC group of
275 atmospheric particles. The last growth type for the SPRM-ARI result is for the cases where
276 the shape of split circular spots had obviously changed during the hygroscopic growth, *i.e.*,
277 the intensity of the spots had become bright and the split segments of the spots had merged,
278 indicating that the particle size has obviously changed. No obvious phase transition of the
279 particle was however observed during the hygroscopic growth of particles in this last
280 growth types, *i.e.*, no obvious deliquescence relative humidity (DRH) detected. The GF
281 was 1.4 when the RH reached 90%. Particles in the last growth type should be in the
282 AS+OC group of atmospheric particles and the deliquescence of the AS has obviously been
283 affected by the presence of liquid OC.

284 Subsequently, the 100nm bulk hygroscopic growth was analyzed synchronously by
285 HTDMA at 84% RH (*i.e.*, after the hygroscopic growth Fig4). The particle size
286 distributions of 100nm EC/fly ash, OC, and AS+OC particles after the hygroscopic growth,
287 calculated using the measured GF, were also shown in the same figure. The HTDMA-
288 measured size distribution was also fitted by the linear combination of the size distributions
289 of EC/Fly ash, OC and AS+OC particles (after the hygroscopic growth), and the result of
290 the fitted size distribution is also given. By the fitting reconstruction, the percentages of
291 EC/Fly ash, OC and AS+OC particles in the HTDMA-measured size distribution can be
292 obtained. It is found that 100 nm atmospheric particles primarily consisted of OC and
293 AS+OC particles, and the ratios of OC and AS+OC particle areas were 45.9% and 47.1%,



294 respectively.

295 In this part of the study, we classified the 100 nm atmospheric particles into four groups
296 using the SEM images and EDS spectrum on September 28th, 2021. The GFs of these
297 nanoparticles had then been measured by *in situ* SPRM-ARI and HTDMA. The
298 hygroscopic growth of these 100nm particles in different groups can be observed at the
299 ambient pressure by the SEM and SPRM-ARI techniques, and the proportion of different
300 groups can be obtained by HTDMA peak fitting reconstruction.

301 **3.2 Size-dependence of SPRM-HTDMA derived chemical composition.**

302 Figure 5 and Figure 6 shows the SEM and SPRM-ARI results of atmospheric particles in
303 the 150 nm and 200 nm size on September 28th, 2021, and their associated EDS mapping
304 results are given in Figure S5-S6. Like the 100 nm atmospheric particles, 150nm and
305 200nm atmospheric particles can also be classified into four groups according to their
306 SEM+EDS mapping results. Compared with the results for the 100 nm atmospheric
307 nanoparticles, no obvious difference in each group was found. The only observable
308 changes were found in the SEM images of particles in the fly ash and AS+OC groups. The
309 clustering status of particles in the fly ash group and the asymmetric shell structure of
310 particles in the AS+OC group becomes very obvious. Especially for 200 nm particles, the
311 AS was found only at the center of these particles (while the OC was widely distributed).

312 Figure 5b and 6b shows the SPRM-ARI results for 150nm and 200nm atmospheric
313 particles. The SPRM imaging results of these particles (shown in Figure S6 and S8) can
314 also be grouped into three growth types: no obvious gray signal change for EC/fly ash
315 nanoparticles; the gray signal enhancement but no obvious shape change in the gray
316 circular spots for OC nanoparticles; and gray signal enhancements and clear shape fusion
317 for AS+OC nanoparticles. When compared with the SPRM-ARI results of 100 nm particles,
318 no observable change in those EC/fly ash and OC particles. However, for the AS+OC
319 particles, their hygroscopic GF decreased as the particle size increased, particularly in the
320 high RH range (>80%). Especially for 200nm AS+OC particles, the GF at the 90% RH



321 decreased from 1.58 to 1.46. Combined with SEM images and EDS mapping results, he
322 reason for the decrease of GF may be the gradual increase of organic content in AS+OC
323 particles.

324 To clearly show the growth trend of AS+OC particles, the kappa (κ) values for the
325 particle sizes of 100-200 nm were calculated at 84% RH (given in Figure 7). At the 84%
326 RH, AS+OC particles would have been completely deliquesced under the assumption of
327 homogeneous liquids. The κ value of pure ammonium sulfate (AS) particles in the same
328 size range was also given. It is found that the change of the κ value for OC and EC/fly
329 ash particles is negligible in the calculated size range. For AS+OC particles, the κ value
330 decreases with the increase of particle size, which indicates that the proportion of organic
331 components (OCs) contained in these particles gradually increases. Thus, the above
332 observation of the κ value for AS+OC particles further confirms that, in the studied size
333 range of the aggregates (100-200 nm), the OC was grown on the sulfate core by the
334 adsorption and condensation.

335 Subsequently, the HTDMA was also used to analyze bulk hygroscopic growth of 150nm
336 and 200nm atmospheric particles at 84% RH, and the hygroscopic particle size spectrum
337 was fitted and reconstructed (Figure 8). It can be see that, as the dry atmospheric particle
338 size increased, the peak separation for OC and AS+OC particles after the hygroscopic
339 growth have changed obviously. The percentage of OC particles in selected atmospheric
340 particles gradually increased and reached 78.2% for 200 nm atmospheric particles. And,
341 the percentage of AS+OC particles in selected atmospheric particles gradually decreased
342 and, *i.e.*, most of AS+OC nanoparticles occurred at the border between the Aitken (10 nm-
343 100 nm) and the condensation modes (100 nm-300 nm). The increase of the OC content in
344 AS+OC particles observed in both the SEM and SPRM measurements also concluded in
345 the HTDMA analysis, *i.e.*, the AS+OC hygroscopic particle peak moved to small particle
346 size as the increase of the dry particle size, which also indicated that OC an important role
347 in the AS+OC nanoparticles growth.



348 **3.3 Comparisons of OC, EC and SO₄⁻**

349 In order to determine the feasibility of combining SPRM atmospheric single nanoparticle
350 test results with HTDMA to evaluate OC, EC and AS+OC contents, the atmospheric
351 nanoparticle hygroscopic growth characteristics on March 22, 2022 have been tested again,
352 and the OC, EC and SO₄⁻ content of different particle sizes were quantitatively analyzed.
353 Figure S9 was the SPRM test results of 100nm, 150nm and 200nm single-particle
354 hygroscopic growth. It can be seen that the atmospheric particulates can also be divided
355 into three categories according to the hygroscopic capacity: EC/flyash without hygroscopic
356 growth, OC with weak hygroscopic growth, and AS+OC with strong hygroscopic growth,
357 and with the increase of particle size, the hygroscopic capacity of AS+OC nanoparticles
358 decreased gradually. Comparing the hygroscopic growth results of atmospheric
359 nanoparticles in two days, we found the GF of AS+OC nanoparticles on March 22, 2022
360 was higher, which may be due to the more SO₄⁻ content of the mixed particles in this
361 experiment. Then, based on the SPRM measurement results, the HTDMA hygroscopic
362 particle size spectrum in the same period could also be divided into three normal
363 distribution peaks (figure S10) and the GF results of SPRM are consistent with the peak
364 position of HTDMA at RH84%. Compared with fitting results on September 22, 2021, the
365 number concentration of atmospheric nanoparticles on March 22, 2022 was lower, and the
366 peak distribution of the three categories were relatively independent. According to the peak
367 area ratio, we found, with the increase of particle size, the proportion of EC was basically
368 about 14%, the proportion of OC gradually increased from 20% to 29%, and the content of
369 AS+OC gradually decreases from 65% to 56.4%, which indicated that the condensation of
370 OC could play an adhesive role in the growth of AS+OC nanoparticles. Subsequently, by
371 measuring the EC, OC and SO₄⁻ contents of nanoparticles collected by the quartz film at
372 the same period (Figure 9), we found, with the increase of particle size, the OC content
373 increased from 33% to 41.8%, and the SO₄⁻ content decreased from 56% to 46.96%. In
374 contrast, the OC content obtained by HTDMA peak splitting method was slightly less than



375 that of the quartz film sampling, which may be due to the OC content obtained by quartz
376 film have included OC in AS+OC category and OC without hygroscopic capacity in
377 EC/flyash category (such as dicarboxylic acid nanoparticles). Comparing the HTDMA
378 peak fitting results and the quartz film sampling results, the analysis method based on the
379 classification of particle hygroscopic characteristics is reliable, which may be helpful to
380 analyze the hygroscopic contribution and growth mechanism of different types
381 atmospheric nanoparticles.

382

383 **4. Conclusions**

384 The measurement of the hygroscopic growth of single nanoparticles is important for the
385 analysis of the chemical composition and hygroscopic characteristics of atmospheric
386 particles, and for the scientific studies involving atmospheric particles. The SPRM imaging
387 technology offers its advantages in the hygroscopic growth measurement of single
388 nanoparticles over the existing methods (e.g., SEM and AFM), particularly for irregular
389 shaped particles. It is because the gray signal of the SPRM-ARI imaging can be positively
390 correlated with the volume of the imaged particles.

391 In this work, atmospheric nanoparticles in the electrical mobility sizes of 100, 150 and
392 200 nm were classified by a DMA and collected for both single-particle and bulk
393 hygroscopic growth measurements. For single-particle measurements, based on the SEM-
394 EDS data, atmospheric particles in a selected size could be grouped into four enabled as
395 EC, fly ash, OC and AS+OC groups. The hygroscopic growth factor of particles in each
396 above group were measured by the SPRM-ARI, and the hygroscopic growth of
397 atmospheric particles due to the very minor change in the chemical composition (e.g., AS+
398 OC particles) could be detected by the above measurements.

399 For bulk hygroscopic growth measurement, this work further demonstrates that the
400 HTDMA-measured size distribution of atmospheric particles at a high RH (i.e., after the
401 hygroscopic growth) could be reconstructed by the linear combination of the calculated



402 size distributions of constitutive particles at a high RH. Besides, the HTDMA peak fitting
403 experiment on March 22, 2022 shows that there was a good correlation between the method
404 of HTDMA peak fitting reconstruction and the quartz film sampling. And, the experimental
405 results of atmospheric nanoparticles hygroscopic growth for two days show that the OC
406 condensation plays an important role in the growth of AS+OC nanoparticles. This
407 reconstruction method has potential significance in predicting the contribution of
408 atmospheric particulate hygroscopicity and particle growth mechanism.

409

410 **Author contributions**

411 **Zhibo Xie:** Methodology, Validation, Visualization, Writing – original draft, Writing –
412 review & editing. **Huaqiao Gui:** Conceptualization, Resources. **Jiaoshi Zhang:** Funding
413 acquisition, Methodology. **Yang Liu:** Methodology. **Bo Yang:** Investigation. **Haosheng**
414 **Dai:** Data curation. **Hang Xiao:** Visualization. **Douguo Zhang:** Methodology, Writing –
415 original draft, Investigation. **Da-Ren Chen:** Conceptualization, Validation. **Jianguo Liu:**
416 Conceptualization, Resources, Funding acquisition.

417

418 **Competing Interest**

419 The authors declare no competing financial interest.

420

421 **Financial support**

422 This work was supported by the National Natural Science Foundation of China (41905028,
423 91544218), the National Key R&D Program of China (2017YFC0209504), the Science
424 and Technological Fund of Anhui Province (1908085MD114, 2108085MD139), and the
425 HFIPS Director's Fund (Nos. YZJJ2022QN04, BJPY2021A04).

426

427 **Supplement**

428 Figures S1–S10 are described in the text (a PDF is available).

429



430 References

- 431 Sloane, C., Wolff, G., 1985. Prediction of ambient light scattering using a physical model responsive to
432 relative humidity: Validation with measurements from detroit. *Atmos. Environ.* 19, 669-680.
433 [https://doi.org/10.1016/0004-6981\(85\)90046-0](https://doi.org/10.1016/0004-6981(85)90046-0).
- 434 Penner, J., Charlson, R., Hales, J., Laulainen, N., Novakov, R., Radke, J., Schwartz, S., Travis, L., 1993.
435 Quantifying and Minimizing Uncertainty of Climate Forcing by Anthropogenic Aerosols. *Bull. Amer.*
436 *Meteor. Soc.* 75, 375-400. [https://doi.org/10.1175/1520-0477\(1994\)075<0375:QAMUOC>2.0.CO;2](https://doi.org/10.1175/1520-0477(1994)075<0375:QAMUOC>2.0.CO;2).
- 437 Abbatt, J., Broekhuizen, K., Pradeepkumar, P., 2005. Cloud condensation nucleus activity of internally mixed
438 ammonium sulfate/organic acid aerosol particles. *Atmos. Environ.* 39, 4767-4778.
439 <https://doi.org/10.1016/j.atmosenv.2005.04.029>.
- 440 Shi, Y., Ge, M., Wang, W., 2012. Hygroscopicity of internally mixed aerosol particles containing benzoic
441 acid and inorganic salts. *Atmos. Environ.* 60, 9-17. <https://doi.org/10.1016/j.atmosenv.2012.06.034>.
- 442 Pilinis, C., Pandis, S., Seinfeld, J., 1995. Sensitivity of direct climate forcing by atmospheric aerosols to
443 aerosol size and composition. *J. Geophys. Res.* 100, 18739-18754. <https://doi.org/10.1029/95JD02119>.
- 444 Agarwal, S., Aggarwal, S. G., Okuzawa, K., Kawamura, K., 2010. Size distributions of dicarboxylic
445 acids, ketoacids, α -dicarbonyls, sugars, WSOC, OC, EC and inorganic ions in atmospheric particles
446 over Northern Japan: implication for long-range transport of Siberian biomass burning and East Asian
447 polluted aerosols. *Atmos. Chem. Phys.* 10, 5839-5858. <https://doi.org/10.5194/acp-10-5839-2010>.
- 448 Fan, j., Rosenfeld, D., Zhang, Y., Giangrande, S., Li, Z., MaChado, L., Martin, S., Yang, Y., Wang, J.,
449 Artaxo, P., Barbosa, H., Braga, R., Comstock, J., Feng, Z., Gao, W., Gomes, H., Mei, F., Pöhlker, C.,
450 Pöhlker, M., Pöschl, U., Souza, R., 2018. Substantial convection and precipitation enhancements by
451 ultrafine aerosol particles. *Science*. 359, 411-418. <https://doi.org/10.1126/science.aan8461>.
- 452 Tan, H., Cai, M., Fan, Q., Liu, L., Li, F., Chan, P. W., Deng, X., Wu, D., 2017. An analysis of aerosol liquid
453 water content and related impact factors in Pearl River Delta. *Sci. Total. Environ.* 579, 1822-1830.
454 <https://doi.org/10.1016/j.scitotenv.2016.11.167>.
- 455 Lei, T., Zuend, A., Wang, W. G., Zhang, Y. H., Ge, M. F., 2014. Hygroscopicity of organic compounds from
456 biomass burning and their influence on the water uptake of mixed organic ammonium sulfate aerosols.
457 *Atmos. Chem. Phys.* 14, 11165-11183. <https://doi.org/10.5194/acp-14-11165-2014>.
- 458 Lei, T., Zuend, A., Cheng, Y., Su, H., Wang, W., Ge, M., 2018. Hygroscopicity of organic surrogate
459 compounds from biomass burning and their effect on the efflorescence of ammonium sulfate in mixed
460 aerosol particles. *Atmos. Chem. Phys.* 18, 1045-1064. <https://doi.org/10.5194/acp-18-1045-2018>.
- 461 Morris, H. S., Estillore, A. D., Laskina, O., Grassian, V. H., Tivanski, A. V., 2016. Quantifying the
462 Hygroscopic Growth of Individual Submicrometer Particles with Atomic Force Microscopy. *Anal. Chem.*
463 88, 3647-3654. <https://doi.org/10.1021/acs.analchem.5b04349>.
- 464 Krieger, U. K., Marcolli, C., Reid, J. P., 2012. ChemInform Abstract: Exploring the Complexity of Aerosol
465 Particle Properties and Processes Using Single Particles Techniques. *Chem. Soc. Rev.* 41, 6631-6662.
466 <https://doi.org/10.1002/chin.201248273>.
- 467 Hiranuma, N., Brooks, S. D., Auvermann, B. W., Littleton, R., 2008. Using environmental scanning electron
468 microscopy to determine the hygroscopic properties of agricultural aerosols. *Atmos. Environ.* 42, 1983-
469 1994. <https://doi.org/10.1016/j.atmosenv.2007.12.003>.



- 470 Peng, C., Chan, M., Chan, C., 2001. The Hygroscopic Properties of Dicarboxylic and Multifunctional Acids:
471 Measurements and UNIFAC Predictions. *Environ. Sci. Technol.* 35, 4495-4501.
472 <https://doi.org/10.1021/es0107531>.
- 473 Ebert, M., Inerle-Hof, M., Weinbruch, S., 2002. Environmental scanning electron microscopy as a new
474 technique to determine the hygroscopic behaviour of individual aerosol particles. *Atmos. Environ.* 36,
475 5909-5916. [https://doi.org/10.1016/S1352-2310\(02\)00774-4](https://doi.org/10.1016/S1352-2310(02)00774-4).
- 476 Gupta, D., Eom, H. J., Cho, H. R., Ro, C. U., 2015. Hygroscopic behavior of NaCl–MgCl₂ mixture particles
477 as nascent sea-spray aerosol surrogates and observation of efflorescence during humidification. *Atmos.*
478 *Chem. Phys.* 15, 11273-11290. <https://doi.org/10.5194/acp-15-11273-2015>.
- 479 Craig, R. L., Bondy, A. L., Ault, A. P., 2015. Surface Enhanced Raman Spectroscopy Enables Observations
480 of Previously Undetectable Secondary Organic Aerosol Components at the Individual Particle Level. *Anal.*
481 *Chem.* 87(15),7510-7514. <https://doi.org/10.1021/acs.analchem.5b01507>.
- 482 Gen, M., Chan, C. K., 2017. Electrospray surface-enhanced Raman spectroscopy (ES-SERS) for probing
483 surface chemical compositions of atmospherically relevant particles. *Atmos. Chem. Phys.* 17(22), 14025-
484 14037. <https://doi.org/10.5194/acp-17-14025-2017>.
- 485 Harmon, C. W., Grimm, R. L., McIntire, T. M., Peterson, M. D., Njagic, B., Angel, V. M., Alshawa, A.,
486 Underwood, J. S., Tobias, D. J., Gerber, R. B., Gordon, M. S., Hemminger, J. C., Nizkorodov, S. A., 2010.
487 Hygroscopic growth and deliquescence of NaCl nanoparticles mixed with surfactant SDS. *J. Phys. Chem.*
488 *B.* 114, 2435-2449. <https://doi.org/10.1021/jp909661q>.
- 489 Morris, H. S., Grassian, V. H., Tivanski, A. V., 2015. Humidity-dependent surface tension measurements of
490 individual inorganic and organic submicrometre liquid particles. *Chem. Sci.* 6, 3242- 3247.
491 <https://doi.org/10.1039/c4sc03716b>.
- 492 Braun C., Krieger U. K., 2001. Two-dimensional angular light-scattering in aqueous NaCl single aerosol
493 particles during deliquescence and efflorescence. *Opt. Express.* 8(6), 314-321.
494 <https://doi.org/10.1364/OE.8.000314>.
- 495 Lv, X. J., Wang, Y., Cai, C., Pang, S. F., Ma, J. B., Zhang, Y. H., 2018. Investigation of gel formation and
496 volatilization of acetate acid in magnesium acetate droplets by the optical tweezers. *Spectrochim Acta A*
497 *Mol. Biomol. Spectrosc.* 200, 179-185. <https://doi.org/10.1016/j.saa.2018.04.027>.
- 498 Li, R., Hu, Y., Li, L., Fu, H., Chen, J., 2017. Real-time aerosol optical properties, morphology and mixing
499 states under clear, haze and fog episodes in the summer of urban Beijing. *Atmos. Chem. Phys.* 17, 5079-
500 5093. <https://doi.org/10.5194/acp-17-5079-2017>.
- 501 Mikhailov, E. F., Mironov, G. N., Pöhlker, C., Chi, X., Krüger, M. L., Shiraiwa, M., Förster, J. D., Pöschl, U.,
502 Vlasenko, S. S., Ryshkevich, T. I., Weigand, M., Kilcoyne, A. L. D., Andreae, M. O., 2015. Chemical
503 composition, microstructure, and hygroscopic properties of aerosol particles at the Zotino Tall Tower
504 Observatory (ZOTTO), Siberia, during a summer campaign. *Atmos. Chem. Phys.* 15, 8847-8869.
505 <https://doi.org/10.5194/acp-15-8847-2015>.
- 506 Wang, S., Shan, X., Patel, U., Huang, X., Lu, J., Li, J., Tao, N., 2010. Label-free imaging, detection, and mass
507 measurement of single viruses by surface plasmon resonance. *Proc. Natl. Acad. Sci. U S A.* 107, 16028-
508 16032. <https://doi.org/10.1073/pnas.1005264107>.
- 509 Huang, B., Yu, F., Zare, R., 2007. Surface Plasmon Resonance Imaging Using a High Numerical Aperture
510 Microscope Objective. *Anal. Chem.* 79, 2979-2983. <https://doi.org/10.1021/ac062284x>.



- 511 Young, G., Hundt, N., Cole, D., Fineberg, A., Andrecka, J., Tyler, A., Olerinyova, A., Ansari, A., Marklund,
512 E., Collier, M., Chandler, S., Tkachenko, O., Allen, J., Crispin, M., Billington, N., Takagi, Y., Sellers, J.,
513 Eichmann, C., Selenko, P., Frey, L., Benesch, J., Kukura, P., 2018. Quantitative mass imaging of single
514 biological macromolecules. *Science* 360, 423-427. <https://doi.org/10.1126/science.aar5839>.
- 515 Halpern, A., Wood, J., Wang, Y., Corn, R., 2014. Single-Nanoparticle Near-Infrared Surface Plasmon
516 Resonance Microscopy for Real-Time Measurements of DNA Hybridization Adsorption. *ACS Nano*. 8,
517 1022-1030. <https://doi.org/10.1021/nn405868e>.
- 518 Syal, K., Iriya, R., Yang, Y., Yu, H., Wang, S., Haydel, S. E., Chen, H. Y., Tao, N., 2016. Antimicrobial
519 Susceptibility Test with Plasmonic Imaging and Tracking of Single Bacterial Motions on Nanometer Scale.
520 *ACS Nano*. 10, 845-852. <https://doi.org/10.1021/acs.nano.5b05944>.
- 521 Maley, A. M., Terada, Y., Onogi, S., Shea, K. J., Miura, Y., Corn, R. M., 2016. Measuring Protein Binding to
522 Individual Hydrogel Nanoparticles with Single-Nanoparticle Surface Plasmon Resonance Imaging
523 Microscopy. *J. Phys. Chem. C*. 120, 16843-16849. <https://doi.org/10.1021/acs.jpcc.6b05700>.
- 524 Wang, W., Yang, Y., Wang, S., Nagaraj, V. J., Liu, Q., Wu, J., Tao, N., 2012. Label-free measuring and
525 mapping of binding kinetics of membrane proteins in single living cells. *Nat. Chem.* 4, 846-853.
526 <https://doi.org/10.1038/NCHEM.1434>.
- 527 Fang, Y., Wang, H., Yu, H., Liu, X., Wang, W., Chen, H. Y., Tao, N. J., 2016. Plasmonic Imaging of
528 Electrochemical Reactions of Single Nanoparticles. *Acc. Chem. Res.* 49 (11), 2614-2624.
529 <https://doi.org/10.1021/acs.accounts.6b00348>.
- 530 Kuai, Y., Chen, J., Tang, X., Xiang, Y., Lu, F., Kuang, C., Xu, L., Shen, W., Cheng, J., Gui, H., Zou, G., Wang,
531 P., Ming, H., Liu, J., Liu, X., Lakowicz, J., Zhang, D., 2019. Label-free surface-sensitive photonic
532 microscopy with high spatial resolution using azimuthal rotation illumination. *Sci. Adv.* 5, 1-10.
533 <https://doi.org/10.1126/sciadv.aav5335>.
- 534 Xie, Z., Kuai, Y., Liu, J., Gui, H., Zhang, J., Dai, H., Xiao, H., Chen, D., Zhang, D., 2020. In Situ Quantitative
535 Observation of Hygroscopic Growth of Single Nanoparticle Aerosol by Surface Plasmon Resonance
536 Microscopy. *Anal. Chem.* 92(16), 11062-11071. <https://doi.org/10.1021/acs.analchem.0c00431>.
- 537 Kuai, Y., Xie, Z., Chen, J., Gui, H., Xu, L., Kuang, C., Kuang, C., Wang, P., Xu, L., Liu, J., Lakowicz, J.,
538 Zhang, D., 2020. Real-Time Measurement of the Hygroscopic Growth Dynamics of Single Aerosol
539 Nanoparticles with Bloch Surface Wave Microscopy. *ACS Nano*. 14(7), 9136-9144.
540 <https://doi.org/10.1021/acs.nano.0c04513>.
- 541 Huang, B., Yu, F., Zare, R., 2007. Surface Plasmon Resonance Imaging Using a High Numerical Aperture
542 Microscope Objective. *Anal. Chem.* 79, 2979-2983. <https://doi.org/10.1021/ac062284x>.
- 543 Petters, M. D., Kreidenweis, S. M., 2007. A single parameter representation of hygroscopic growth and cloud
544 condensation nucleus activity. *Atmos. Chem. Phys.* 7, 1961-1971. <https://doi.org/10.5194/acp-7-1961-2007>.
- 546 Fan, X., Liu, J., Zhang, F., Chen, L., Collins, D., Xu, W., Jin, X., Ren, J., Wang, Y., Wu, H., Li, S., Sun, Y., Li,
547 Z., 2020. Contrasting size-resolved hygroscopicity of fine particles derived by HTDMA and HR-ToF-AMS
548 measurements between summer and winter in Beijing: the impacts of aerosol aging and local emissions.
549 *Atmos. Chem. Phys.* 20, 915-929. <https://doi.org/10.5194/acp-20-915-2020>.
- 550 Jacobson, M. C., Hansson, H. C., Noone, K. J., Charlson, R. J., 2000. Organic atmospheric aerosols: Review
551 and state of the science. *Rev. Geophys.* 38(2), 267-294. <https://doi.org/10.1029/1998RG000045>.



552 Zhang, J., Chen, Z., Lu, Y., Gui, H., Liu, J., Liu, W., Wang, J., Yu, T., Cheng, Y., Chen, Y., Ge, B., Fan, Y.,
553 Luo, X., 2017. Characteristics of aerosol size distribution and vertical backscattering coefficient profile
554 during 2014 APEC in Beijing. *Atmos. Environ.* 148, 30-41.
555 <https://doi.org/10.1016/j.atmosenv.2016.10.020>.

556 Bondy, A., Bonanno, D., Moffet, R., Wang, B., Laskin, A., Ault, A., 2018. The diverse chemical mixing state
557 of aerosol particles in the southeastern United States. *Atmos. Chem. Phys.* 18, 12595–12612.
558 <https://doi.org/10.5194/acp-18-12595-2018>.

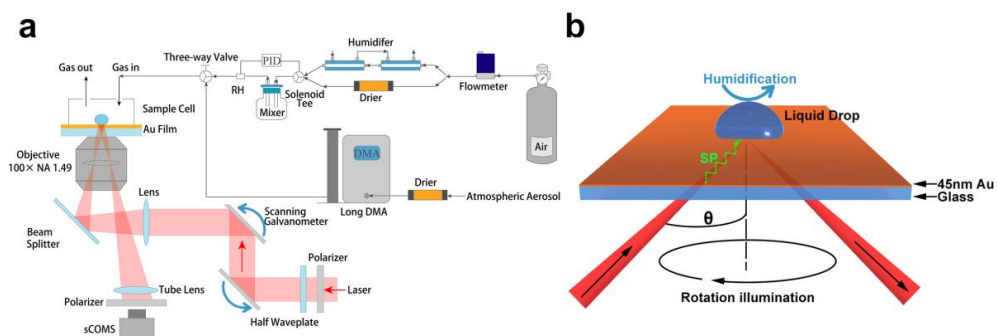
559 Estillore, A., Morris, H., Or, V., Lee, H., Alves, M., Marciano, M., Laskina, O., Qin, Z., Tivanski, A., Grassian,
560 H., 2017. Linking hygroscopicity and the surface microstructure of model inorganic salts, simple and
561 complex carbohydrates, and authentic sea spray aerosol particles. *Phys. Chem. Chem. Phys.* 19(31), 21101-
562 21111. <https://doi.org/10.1039/c7cp04051b>.

563 Chow, J., Waston, J., Chen, L., Arnott, W., Moosmüller, H., Fung, K., 2004. Equivalence of Elemental Carbon
564 by Thermal/Optical Reflectance and Transmittance with Different Temperature Protocols. *Environ. Sci.*
565 *Technol.* 38, 4414-4422.

566 Ding, Q., Liu, J., Lu, Y., Wang, Y., Lu, F., Shi, J., Research and development of an on-line carbonaceous
567 aerosol analyzer. *Chinese Journal of Scientific Instrument*, 35(6), 1246-1253.

568
569
570
571
572
573
574
575
576
577
578
579
580
581
582
583
584
585
586

587 **Figures Caption**

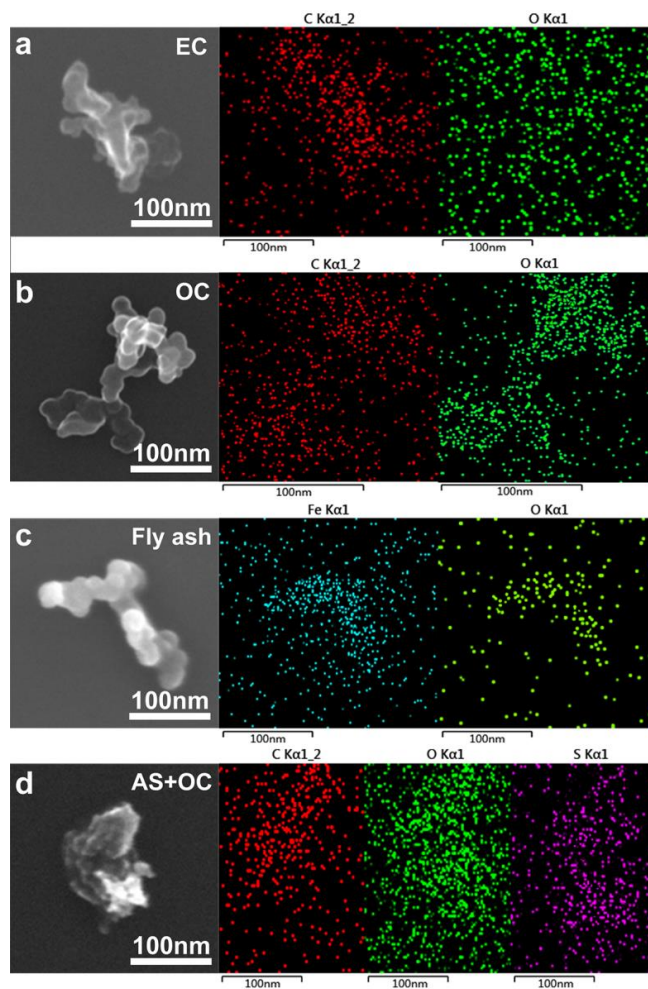


588

589 Figure 1. Schematic diagram of the *in situ* SPRM-ARI single nanoparticle moisture
590 absorption system: (a) for the complete system setup, and (b) for the gold-coated glass

591

substrate used for *in situ* SPRM-ARI.

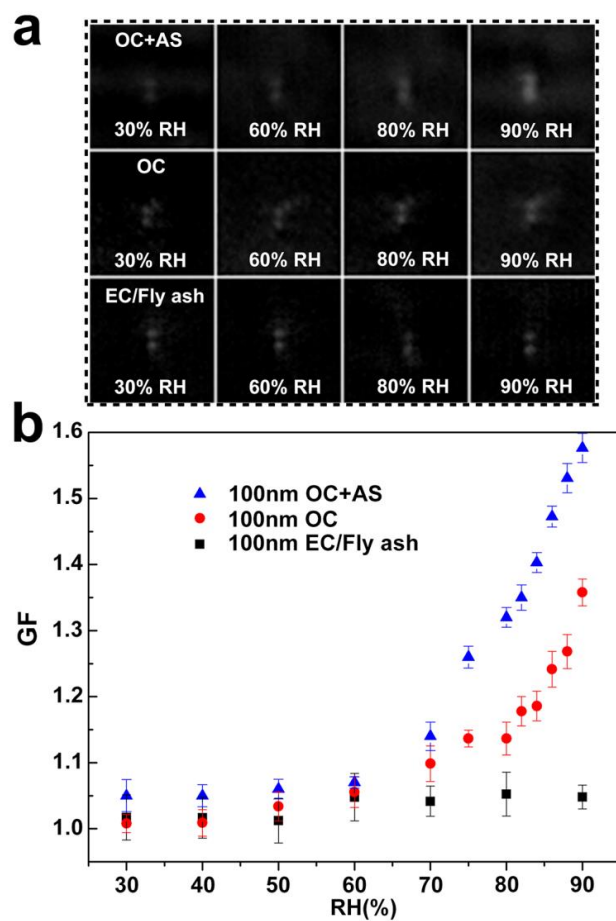


592

593 Figure 2. SEM and EDS mapping of typical 100 nm atmospheric particles collected in

594

this study.

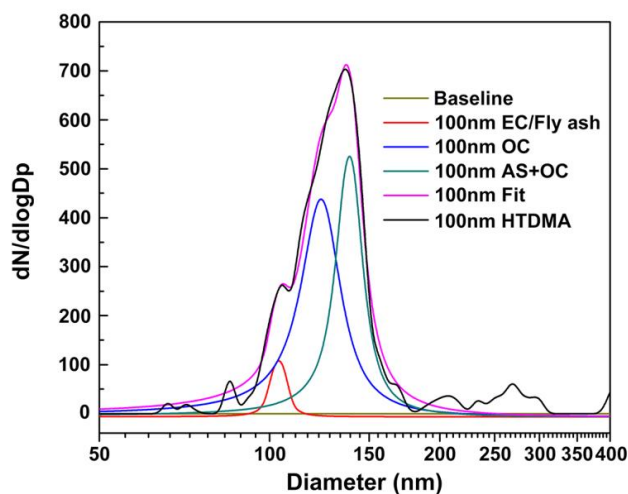


595

596

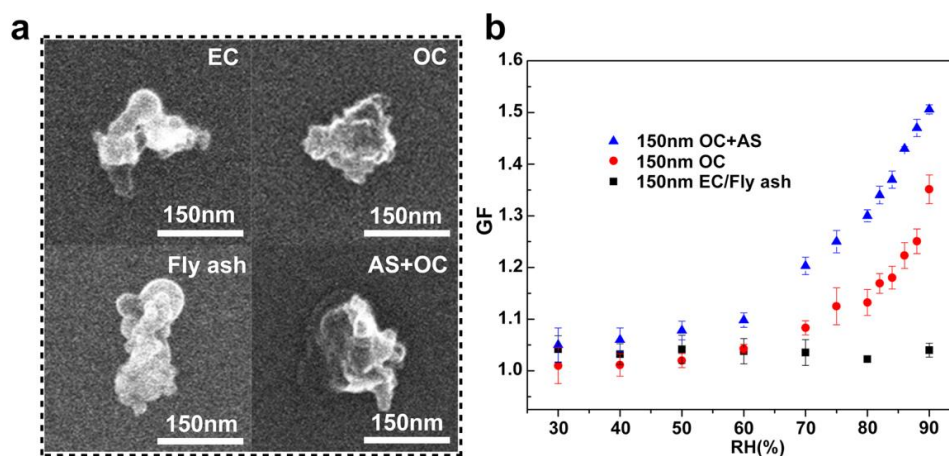
597

Figure 3. (a) SPRM-ARI images and (b) hygroscopic growth factors of 100 nm atmospheric particles.



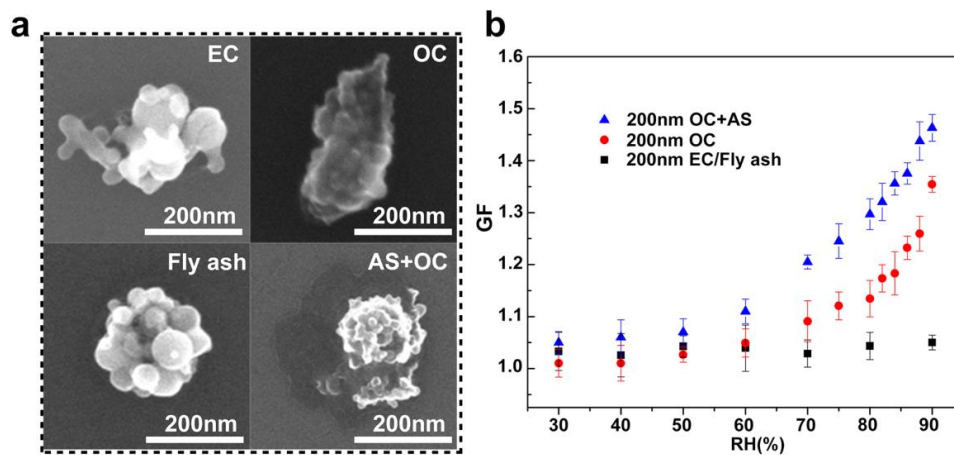
598

599 Figure 4. HTDMA and peak fitting reconstruction for 100 nm atmospheric particles at
600 84% RH on September 28th, 2021.



601

602 Figure 5. (a) SEM images and (b) hygroscopic growth factors of atmospheric particles in
603 the 150 nm size.

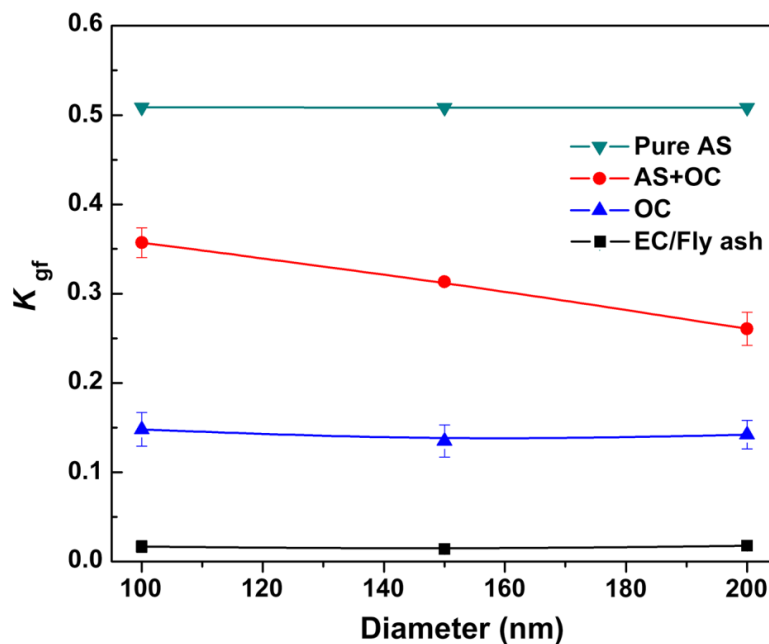


604

605

606

Figure 6. (a) SEM images and (b) hygroscopic growth factors of 200 nm atmospheric particles.

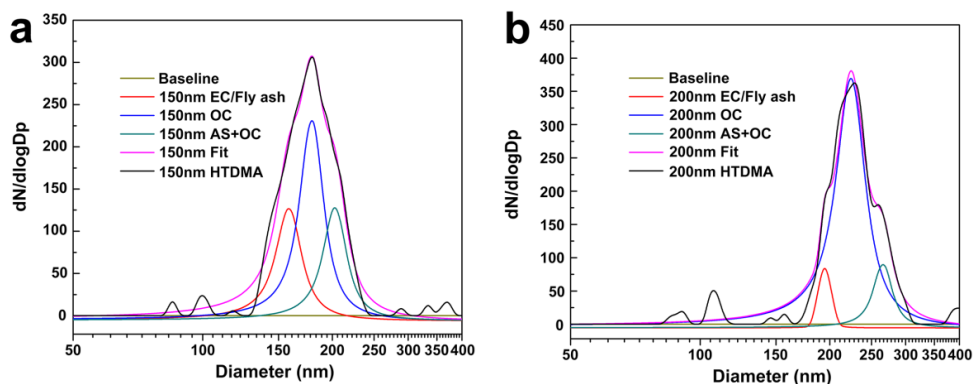


607

608

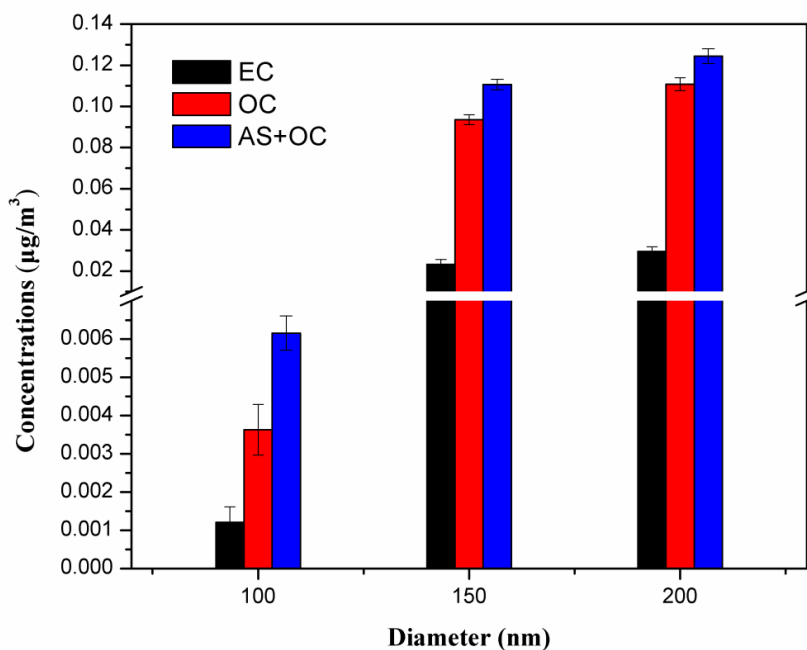
609

Figure 7. κ results for the 100 nm, 150 nm and 200 nm atmospheric particles at RH on September 28th, 2021.



610
611
612

Figure 8. HTDMA and peak fitting reconstruction for (a) 150 nm and (b) 200 nm atmospheric particles at 84% RH on September 28th, 2021.



613
614
615
616

Figure 9. Quantitative results of atmospheric nanoparticles subgroups collected by quartz filter membrane on March 22th, 2022.